Absorption and transport of hydrogen during gas metal arc welding of low alloy steel

K. Mundra, J. M. Blackburn, and T. DebRoy

Although hydrogen induced cracking remains a major problem in the welding of steels, the present methods of managing hydrogen in the weldment are mostly empirical in nature. In recent years, numerical modelling of heat transfer and fluid flow has provided detailed insight into the physical processes in welding. However, very little effort has been made in the past to use these transport phenomena based calculations to understand the dissolution of hydrogen in the weld metal and its subsequent transport in the liquid and solid regions. The aim of the present work was to address this important need. Heat transfer, fluid flow, and hydrogen transport calculations in transient, three-dimensional form are used to predict the spatial distribution of hydrogen concentration in the weld metal during gas metal arc welding of mild steels for different welding conditions. The enhanced hydrogen solubility in the weld metal above that predicted by Sieverts law was determined from a model for the partitioning of hydrogen between the weldment and its plasma environment. The model considers the presence of a superequilibrium concentration of atomic hydrogen which is significantly higher than that produced by thermal dissociation. The results indicate that for a meaningful prediction of the hydrogen concentration in the weld metal, hydrogen absorption at the weld pool surface, transport of hydrogen within the weld pool, and the diffusion of hydrogen away from the solidified weld metal should be considered simultaneously. The agreement between the experimental and predicted results indicates significant promise for predicting weld metal hydrogen concentration in fusion welds from fundamentals of transport phenomena.

At the time the work was carried out, Dr Mundra and Professor DebRoy were in the Department of Materials Science and Engineering, the Pennsylvania State University, University Park, PA 16802, USA and Mr Blackburn was at the Naval Surface Warfare Center, Carderock Division, Building 60, Welding Branch, Code 615, Bethesda, MD 20084–5000, USA. Dr Mundra is now with General Electric Corporate Research and Development, 1 Research Circle, Schenectady, NY 12301, USA. *Manuscript received 13 February 1997.*

INTRODUCTION

Hydrogen embrittlement is a major problem in the welding of steels and the present methods used to control hydrogen in the weldment are mostly empirical in nature. Owing to the nature of the fusion welding environment, ions and excited atoms and molecules of hydrogen and other gases are present above the weld pool surface, which leads to enhanced solubility of gaseous species in the weld pool much above that predicted by Sievert's law.[1–4] The extent of absorption of these species depends on the nature and composition of the welding environment, the temperature distribution on the weld pool surface, and the surface area of the weld pool. After hydrogen is absorbed on the surface of the weld pool, it is transported by convection and diffusion to the interior of the weld pool and by diffusion to the interior of the solid metal. As the weld pool cools, some hydrogen is desorbed from the weldment surface, while the diffusion from the weld metal to the interior continues in a transient manner. Therefore, the spatial distribution of hydrogen in the weldment structure is the result of the transient transport of hydrogen over the entire duration of welding.

Most of the previous studies on hydrogen diffusion were undertaken to reduce the hydrogen content through a post-weld heat treatment, rather than to understand the distribution of hydrogen in the weldment during and after the welding process. The diffusion of hydrogen from the weld metal and the heat affected zone is important in determining their final concentrations in the weldment. Terasaki *et al.*[5] calculated the hydrogen diffusion rates in a bead on plate weld metal with a simplified two-dimensional model using Fick's second law and Dickehut and Ruge[6] applied this model when considering the weld bead shape. Boellinghaus *et al.*[7] summarised the previous work on the hydrogen diffusion coefficient, taking into account factors such as porosity, alloying elements, minute impurities, effect of microstructure, and cold work. Boellinghaus *et al.*[8] also calculated hydrogen distribution in the welded joints. However, these studies on modelling of hydrogen contents in the weld metal ignored the effects of the plasma, the absorption of hydrogen on the weld pool surface, and the role of convection in the distribution of hydrogen in the weld pool. Gedeon and Eagar[1] presented a thermodynamic analysis to demonstrate the importance of monatomic hydrogen in the welding environment. Their work represented a major advancement in the understanding of the absorption of hydrogen in the weld pool. However, to understand residual hydrogen in the weldment, further work considering the absorption of hydrogen in the weld pool, the convective transport of hydrogen in the weld pool, and the diffusive transport in the solid region needs to be undertaken.

In the past decade, mathematical modelling of the transport of heat, mass, and momentum in the weld pool has provided significant insight into the welding process that could not have been obtained otherwise. For example, it has been shown[9,10] that the evolution of weld metal geometry of over two hundred welds, in which both the composition of the steels and welding variables were systematically varied, could be satisfactorily modelled. Furthermore, understanding of the role of surface active impurities in the development of weld pool geometry has improved significantly.[9–11] Although the qualitative effects of surface active elements on the development of weld pool geometry have been known since the early 1980s,[12,13] recent modeling work[9,10] has shown that the presence of surface

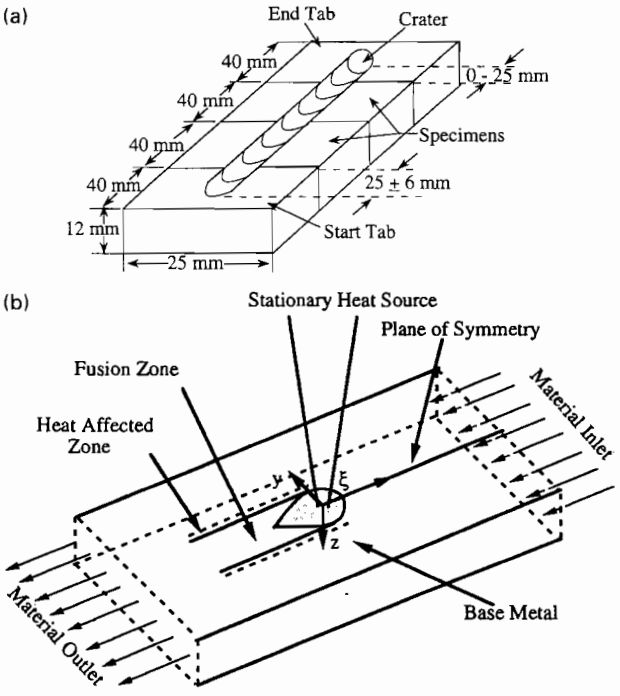

a of diffusible H test specimen; *b* of welding process on coordinate system attached to heat source

1 Schematic diagram

active elements is not a guarantee of achieving a high aspect ratio. Indeed, only when convective heat transport is important, i.e. at high Peclet numbers, can the presence of sulphur lead to a high weld pool aspect ratio. Furthermore, simple features of solidification structure, such as secondary dendrite arm spacings, have been predicted from the cooling rate data calculated from the fundamentals of transport phenomena.[14] However, comprehensive fluid flow and heat transfer calculations have not been used to predict the distribution of interstitial species, such as nitrogen and hydrogen, in the weldment.

The work described in the present paper was aimed at understanding the absorption and transport of hydrogen. Controlled weld metal diffusible hydrogen tests, using gas metal arc welding (GMAW), were performed in the presence of a small amount of hydrogen in the welding environment. A three-dimensional model to calculate heat transfer, fluid flow, and hydrogen concentration in the weldment was applied to predict hydrogen concentration in a low alloy steel weldment; the predicted trend of hydrogen content was consistent with the experimental observations for the conditions investigated. The calculations indicate significant promise for predicting weldment hydrogen content for mild steels from the fundamentals of transport phenomena.

EXPERIMENTAL

Welding experiments were conducted according to AWS Standard A4.3–93 (Ref. 15). Since extensive details of the procedure are available elsewhere,[15] only a brief summary is given here. The test assembly consisted of a starting tab (40 mm), two test specimens (40 mm each), and a runoff weld tab (40 mm), all held in a copper clamping fixture. A schematic diagram of the test specimen is shown in Fig. 1*a*. The width and the thickenss of the test specimen were 25 and 12 mm respectively. The test specimen was degassed and cleaned according to the AWS standard before welding.

The parameters used for welding were:

Process	GMAW
Current, A	300
Voltage, V	27
Welding speed, mm s^{-1}	5·2, 12·7, 23·2
Wire feedrate, mm s^{-1}	93
Wire diameter, mm	1·6
Shielding gas	$98Ar–2O_2$
Amount of H added	1%

The chemical composition of the MIL–E–120S–1 welding wire used in the experiments was Fe–0·07C–0·6Si–(0·905–2·35)Mn–0·12P–0·008S–0·8Cr–(0·3–1·0)Mo–(1·0–3·0)Ni–0·1Al–0·3Cu–0·1Ti–0·038V–0·1Zr, where the amounts of carbon, silicon, phosphorus, sulphur, chromium, aluminium, copper, titanium, and zirconium were the maximum allowed. The arc was initiated on the starting tab at a distance of 25 ± 6 mm from the edge of the test specimen and was terminated on the runoff weld tab at a position such that the back edge of the crater was on the runoff weld tab, but within 25 mm of the edge of the test specimen.

The weld test assembly was released from the copper clamping fixture and plunged into an agitated ice water bath within 5 s of extinguishing the arc. It was then transferred to a low temperature liquid bath (containing acetone and dry ice) within 20 s. After the test assembly had been kept in a low temperature liquid bath for some time, the weld tabs were broken and cleaned with a wire brush.

The cleaned weld specimens were then encapsulated in airtight steel chambers under an argon atmosphere. The steel chambers were then placed in a furnace maintained at 45°C for 72 h, allowing the hydrogen to diffuse out of the specimens. Subsequently, the thermal conductivity of the Ar–H mixture was measured to give the diffusible hydrogen content in the weld specimen.

MATHEMATICAL FORMULATION

Equations of conservation of mass, momentum, energy, and hydrogen concentration

The equations of conservation of mass, momentum, energy, and hydrogen concentration were formulated in a coordinate system attached to the heat source. In this coordinate system, shown schematically in Fig. 1*b*, the heat source and the molten metal under the heat source are fixed in space and the material enters and leaves the computational domain at the welding velocity. Details of the energy, momentum, and hydrogen conservation equations are given in Appendix 1. The quantities ξ, y, and z refer to distance in the welding, specimen width, and specimen depth directions respectively.

Solution of the governing equations in this coordinate system provides several advantages. In the fixed coordinate system, a large number of fine grids are required for accurate representation of the moving, time dependent position of the heat source and the spatial variation of the heat flux. However, in the coordinate system attached to the heat source, the grids can be finer near the heat source and coarser away from the heat source. As a result, there is improved spatial and temporal resolution of the variables. In addition, economy of data storage and improved computational speed are achieved.

Solution procedure

The governing equations were represented in a finite difference form and solved iteratively on a line by line basis using a tridiagonal matrix algorithm (TDMA). The semi-implicit method for pressure linked equations (SIMPLE) algorithm was employed for the discretisation of the equations. Details of the procedure are described elsewhere.[16,17] The model used a 50 × 28 × 26 grid system for the calculation of enthalpies, velocities, and the hydrogen concentration. Spatially non-uniform grids were used for maximum resolution of the variables.

The time dependent solution of the governing equations in three dimensions is time consuming. However, since the

weld pool geometry reaches a steady state in a very short time after the start of welding, the steady state versions of the governing equations were solved for energy and momentum. A fully transient, three-dimensional form of the governing equation was solved for the hydrogen concentration.

Boundary conditions and source terms for momentum equations

Since the temperature varies on the surface of the weld pool, a shear stress (Marangoni stress) is produced on the free surface.[18] The effective tangential stress τ owing to this effect on the free surface was calculated from

$$\tau = (\mathrm{d}\gamma/\mathrm{d}T)\nabla T \quad . \quad . \quad . \quad . \quad . \quad . \quad . \quad . \quad . \quad . \quad . \quad . \quad . \quad (1)$$

where $\mathrm{d}\gamma/\mathrm{d}T$ is the temperature coefficient of surface tension and ∇T is the temperature gradient.

The natural convection effect, i.e. the buoyancy force, is taken into account by defining the buoyancy source term S_b to be

$$S_b = \rho g \beta (T - T_{ref}) \quad . \quad . \quad . \quad . \quad . \quad . \quad . \quad . \quad . \quad . \quad . \quad . \quad (2)$$

where ρ is the density, g is the acceleration owing to gravity, β is the thermal expansion coefficient, and T_{ref} is any arbitrarily selected temperature.

The interaction between the divergent current path in the weld pool and the magnetic field it creates gives rise to electromagnetically driven flow in the pool.[18] The electromagnetic force $\boldsymbol{F}_e$ is given by

$$\boldsymbol{F}_e = \boldsymbol{J} \times \boldsymbol{B} \quad . \quad . \quad . \quad . \quad . \quad . \quad . \quad . \quad . \quad . \quad . \quad . \quad . \quad . \quad (3)$$

where $\boldsymbol{J}$ is the current density vector and $\boldsymbol{B}$ is the magnetic flux vector. Since the heat source is axisymmetric, $\boldsymbol{F}_e$, calculated by the formulation given by Kou and Yang,[19] was incorporated as a source term. The flow in the mushy zone was modelled using the Carman–Kozeny equation.[20,21] Details of the procedure are given in Ref. 22.

Calculations were performed for only half the workpiece because of the symmetry about the $y = 0$ plane (Fig. 1*b*). Along the plane of symmetry, the flux of u and w (the components of velocity in the ξ and z directions) and v (the component of velocity in the y direction) were assumed to be zero. Since the weld pool surface was assumed to be flat, w was defined to be zero at the top surface. Owing to the complexities involved in the complete modelling of the droplet transfer to the weld pool, momentum transfer to the weld pool from the droplets was neglected in the calculation. It is shown below that the fluid flow caused by Marangoni stress is sufficiently strong, giving rise to a high Peclet number for heat Pe_h and for mass transfer Pe_m in the weld pool. As a consequence, incorporation of the momentum transfer from the droplet may have only a small influence on the heat and mass transfer in the weld pool.

Boundary conditions for energy equation

In the GMAW process, heat transfer to the workpiece takes place from both the arc and the metal droplets. The heat transfer from the arc J_h was assumed to be Gaussian in nature and was prescribed on the top surface according to the equation

$$J_h(\xi, y, z)_{z=0} = (3Q\eta/\pi r_b^2) \exp[-3(\xi^2 + y^2)/r_b^2] \quad . \quad . \quad (4)$$

where Q is the power input (current × voltage), η is the process efficiency, and r_b is the arc radius.

In addition to heat transfer from the arc, energy is also transferred to the workpiece from the metal droplets generated from the consumable electrode. The energy transfer from the droplets depends on various parameters such as the drop frequency, the drop transfer mode, and the shape, size, and temperature of the droplets. Owing to the inherent complexities in the measurement of these parameters, experimental data on these parameters are limited. Theoretical models for the calculation of drop characteristics are still developing.[23] Therefore, in the present work, heat transfer by the metal droplets was taken into account by inserting a volumetric heat source in the weld pool. The procedures for calculating the dimensions of the volumetric heat source are described elsewhere.[24] In the present calculations, the radius and the depth of the volumetric heat source were taken to be 1 and 3 mm respectively, based on the available data.[24]

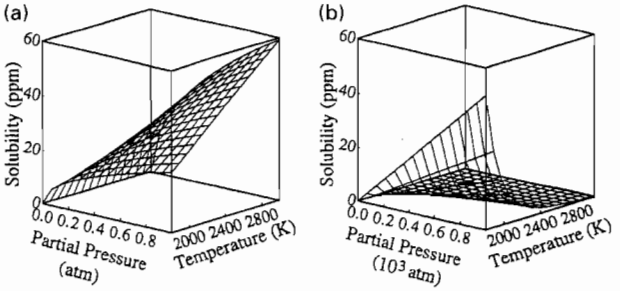

1 atm = $1{\cdot}013 \times 10^5$ Pa
a exposed to diatomic H; *b* exposed to monatomic H

2 Equilibrium solubility of H in Fe as function of temperature and pressure

The total power was 8100 J s^{-1}, while the overall efficiency of the process was assumed to be 80% (~6480 J s^{-1}).[25] From the wire feedrate and the diameter of the wire, listed above, the volume of the metal deposited from the droplets was $18{\cdot}5 \times 10^{-8}$ m^3 s^{-1}. Assuming a density of 7200 kg m^{-3}, $\sim 1{\cdot}33 \times 10^{-3}$ kg of metal was deposited from the droplets every second. The droplets, assumed to be at a temperature of 2773 K, carried an energy of ~1881 kJ kg^{-1}. Thus, ~2500 J of heat (~40% of the total absorbed energy) will have come from the metal drops each second. The remaining 60% of the energy came from the arc. The energy coming from the droplets was assumed to be uniformly distributed in the cylindrical cavity.

At the plane of symmetry, the gradient of enthalpy ($\mathrm{d}H/\mathrm{d}y$) was assumed to be zero. At the other surfaces of the specimen (copper block), the temperature was prescribed as room temperature, 298 K.

Boundary conditions for hydrogen conservation

Hydrogen transfer into the weldment originates from both the droplets and from surface absorption and desorption, which is similar to the transport of heat which takes place both from the interaction of the arc and the material and droplet transfer. It is now well established that Sievert's law can not be applied to predict gas concentrations in metals exposed to plasma environments.[1–4,26,27] This is because hydrogen atoms and ions are present in the plasma as well as in diatomic hydrogen molecules in the ground state.

The presence of atomic hydrogen leads to significantly higher hydrogen solubility in the weld metal. This is illustrated in Fig. 2, in which the equilibrium solubility of hydrogen in iron is plotted as a function of temperature and partial pressure, for both monatomic and diatomic hydrogen. It can be seen from Fig. 2 that a low partial pressure of monatomic hydrogen can lead to equilibrium solubilities comparable to that obtained at very high partial pressures of diatomic hydrogen.

A model was used to account for the surface absorption of hydrogen from the monatomic hydrogen.[1,26] A schematic diagram of the model is shown in Fig. 3. The diatomic hydrogen dissociates in the arc at a dissociation temperature T_d, while the monatomic hydrogen is transported to the surface of the weld pool, where it dissolves at a local weld pool surface temperature T_s. Details of the model are given

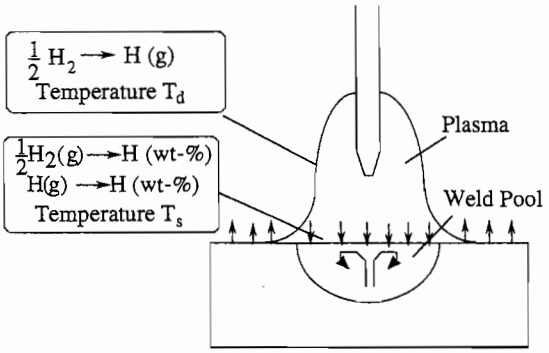

3 Schematic diagram of gas dissolution from plasma in weld pool

in Ref. 26. The T_d value in the plasma depends on many factors, such as the partial pressure of the individual gases, total pressure, arc voltage, and arc current. In the present work, the measured arc temperature data from previously published work of Key *et al.*[28] were used for T_d; data are shown in Fig. 4. Based on these temperatures, the spatial variation of the partial pressure of monatomic hydrogen was calculated. At low temperatures (beyond the plasma), the dissociation of the diatomic hydrogen will be insignificantly small and, under such conditions, the solubility from the diatomic hydrogen could be greater than that from the monatomic hydrogen. Therefore, the solubilities were calculated both from monatomic and diatomic hydrogen and the higher of the two was applied as the boundary condition on the surface of the specimen. However, the upper limit of the solubility obtained from monatomic hydrogen can not exceed the equilibrium solubility corresponding to a pressure of 1×10^5 Pa of diatomic hydrogen. The reason for the upper limit of solubility is that when this solubility is exceeded, hydrogen bubbles nucleate at the surface of the weld pool. Therefore, for a given surface temperature, the hydrogen solubility at the surface was limited by the equilibrium solubility at a 1×10^5 Pa pressure of diatomic hydrogen. In brief, for a given surface temperature, the surface concentration was determined by the method outlined below. For diatomic hydrogen

$$\tfrac{1}{2}H_2(g) = H \qquad (\Delta G_1^\circ)_{T_s} \quad . \quad . \quad . \quad (5)$$

$$(C_H)_d = (p_{H_2})_{T_d}^{1/2} \exp(-\Delta G_1^\circ / RT_s) \quad . \quad . \quad . \quad . \quad . \quad . \quad . \quad (6)$$

where $(C_H)_d$ is the surface concentration owing to diatomic hydrogen in parts per million, $(p_{H_2})_{T_d}$ is the partial pressure of diatomic hydrogen at T_d, ΔG_1° is the standard free energy, and R is the gas constant. For monatomic hydrogen

$$H(g) = H \qquad (\Delta G_2^\circ)_{T_s} \quad . \quad . \quad . \quad (7)$$

$$(C_H)_m = (p_H)_{T_d} \exp(-\Delta G_2^\circ / RT_s) \quad . \quad . \quad . \quad . \quad . \quad . \quad . \quad (8)$$

where $(C_H)_m$ is the surface concentration owing to monatomic hydrogen and $(p_H)_{T_d}$ is the partial pressure of monatomic hydrogen at T_d. The relationship between the

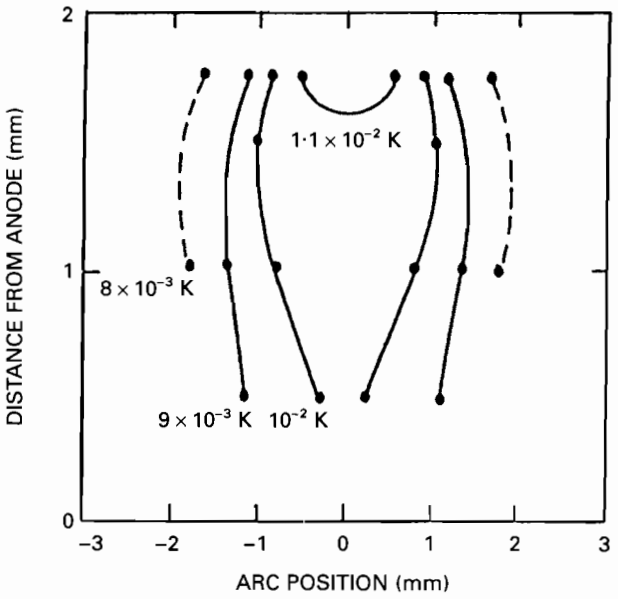

4 Measured arc temperature data: after Key *et al.*[28]

equilibrium values of $(p_{H_2})_{T_d}$ and $(p_H)_{T_d}$ is given by

$$\tfrac{1}{2}H_2(g) = H(g) \qquad (\Delta G_3^\circ)_{T_d} \quad . \quad . \quad . \quad (9)$$

$$p_H = p_{H_2}^{1/2} \exp(-\Delta G_3^\circ / RT_d) \quad . \quad . \quad . \quad . \quad . \quad . \quad . \quad . \quad . \quad . \quad (10)$$

The saturation concentration $(C_H)_s$ is given by

$$(C_H)_s = p_{atm}^{1/2} \exp(-\Delta G_1^\circ / RT_s) \quad . \quad . \quad . \quad . \quad . \quad . \quad . \quad . \quad . \quad (11)$$

where p_{atm} is the atmospheric pressure of 1×10^5 Pa and the surface concentration C_s is

$$C_s = \min\{(C_H)_s, \max[(C_H)_m, (C_H)_d]\} \quad . \quad . \quad . \quad . \quad . \quad (12)$$

It is to be emphasised that in equation (12), the maximum of $(C_H)_d$ and $(C_H)_m$ was taken and applied as the boundary condition. The contributions of $(C_H)_d$ and $(C_H)_m$ were not added. This can be illustrated with an example. Let there be a condition in which the metal–diatomic gas–monatomic gas system is in complete equilibrium. Under this condition, the solubility from both the diatomic and monatomic hydrogen is reached at the same concentration of dissolved hydrogen in the metal, say 3 ppm. If the contributions from both monatomic and diatomic hydrogen are added, the amount of hydrogen dissolved in the metal will be 6 ppm. Therefore, the equilibrium condition for both monatomic and the diatomic hydrogen will be violated. The methodology for prescribing hydrogen concentration on the weldment surface is given in Appendix 2.

In addition to the hydrogen absorption at the surface of the weld pool, a significant amount of hydrogen in the weld metal also comes from the droplets. Droplets pick up a significant amount of hydrogen before impinging on the weld pool surface because they are directly exposed to plasma in the arc column. The amount of hydrogen picked

Table 1 Minimum, maximum, and average values* of diffusion coefficient of hydrogen in microalloyed and low carbon structural steels obtained from Ref. 8

Temperature, K	Diffusion coefficient, $mm^2\ s^{-1}$		
	Minimum	Maximum	Average
293–473	$8{\cdot}7615 \times 10^{-9}(T-273)^{2{\cdot}2285}$	$0{\cdot}076\ e^{-9562/RT}$	$0{\cdot}07465\ e^{-11072/RT}$
473–1013	$8{\cdot}9963 \times 10^{-9}(T-273)^{2{\cdot}2480}$	$8{\cdot}1056 \times 10^{-6}(T-273)^{1{\cdot}2528}$	$0{\cdot}1104\ e^{-12437/RT}$
1013–1723	$0{\cdot}6736\ e^{-45086/RT}$	$1{\cdot}0691\ e^{-41624/RT}$	$0{\cdot}8753\ e^{-46396/RT}$
1723–1823	$28{\cdot}7905\ e^{-93534/RT}$	$0{\cdot}437\ e^{-17273/RT}$	$1{\cdot}2104\ e^{-37785/RT}$
1823–2273	$0{\cdot}246\ e^{-15450/RT}$	$0{\cdot}437\ e^{-17273/RT}$	$1{\cdot}1578\ e^{-37007/RT}$

* $R = 8{\cdot}315$ J K mol^{-1}.

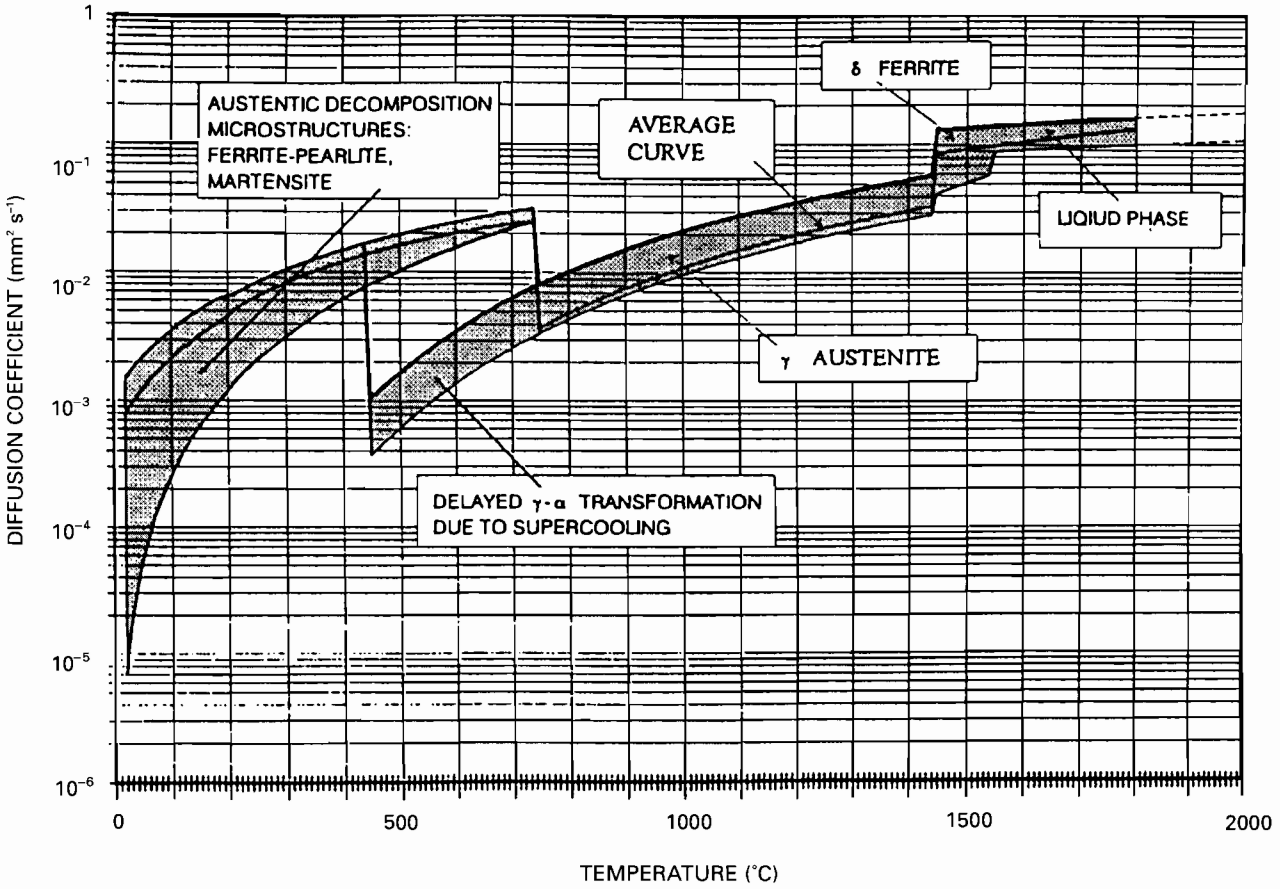

5 Scatterband for H diffusion coefficient: after Boellinghaus *et al.*[8]

up by the droplets depends on factors such as the temperature of the metal drops, the hydrogen content in the shielding gas, and the arc temperature. The concentration of hydrogen in the droplets was calculated as described in the present paper. At the high temperatures characteristic of the arc, complete dissociation of diatomic hydrogen takes place. Indeed, if one considers an arc temperature of 3600 K, 99% of the diatomic hydrogen will be dissociated in a feed gas mixture containing $99Ar–1H_2$. This would lead to a p_H value of $1{\cdot}9 \times 10^3$ Pa in equation (10). Under such conditions, $(C_H)_m$ in the drops at a temperature of 2773 K will tend to reach a value of 12 ppm for equation (8). This value was used as a hydrogen concentration in the droplets, which were assumed to be contained in a cylindrical cavity with the same dimensions as the cavity for the heat source.

At the plane of symmetry, the gradient of hydrogen concentration dC/dy was assumed to be zero. At the other surface of the specimen the hydrogen concentration was prescribed as zero. This is because these surfaces are far from the weld pool surface. Hydrogen diffusion to these surfaces does not occur in the time frame in which welding is carried out. An order of magnitude calculation can be made using

$$x = 2(Dt)^{1/2} \quad \ldots\ldots\ldots\ldots\ldots\ldots \quad (13)$$

where x is the distance at which the concentration falls to about 50%, D is the diffusion coefficient, and t is time. The maximum value of t for which welding is carried out, for the lowest welding velocity case, is 25 s. Taking an average diffusivity of $1{\cdot}0 \times 10^{-2}$ mm^2 s^{-1} at a temperature of 700 K (Fig. 5), the diffusion distance is only 1 mm. Thus, the amount of transport of hydrogen by diffusion alone into the solid part of the weldment is relatively small for the duration of the experiment, i.e. before the specimens are quenched in the ice water bath.

Hydrogen diffusion coefficient

The values of the hydrogen D value, as a function of temperature, are necessary for the solution of the equation of conservation of hydrogen. Boellinghaus *et al.*[7] summarised the previous work on the hydrogen D value by taking into account the 'trapping' of hydrogen owing to various 'inner effects', such as porosity, alloying elements, minute impurities, and the effect of microstructure, cold work, and applied stress. A scatterband of hydrogen D values for micro- and low alloy structural steels was suggested. This scatterband is shown in Fig. 5. An average of the minimum and maximum hydrogen D values, as a function of temperature, was used in the calculations. The equations used are summarised in Table 1.

RESULTS AND DISCUSSION

A typical three-dimensional, steady state temperature field is shown in Fig. 6. The thermophysical properties used in the calculations were:

Density, kg m^{-3}	7200
Solidus temperature, K	1745
Liquidus temperature, K	1785
Viscosity, kg m^{-1} s	0·024
Thermal conductivity of solid iron, J m^{-1} s^{-1} K^{-1}	20·9
Thermal conductivity of liquid iron, J m^{-1} s^{-1} K^{-1}	334
Specific heat of solid iron, J kg^{-1} K^{-1}	702
Specific heat of liquid iron, J kg^{-1} K^{-1}	806
Latent heat of melting of iron, J kg^{-1}	267 000
Thermal conductivity of air, J m^{-1} s^{-1} K^{-1}	$7{\cdot}1 \times 10^{-3}$
Density of air, kg m^{-3}	1·3
Specific heat of air, J kg^{-1} K^{-1}	20 800

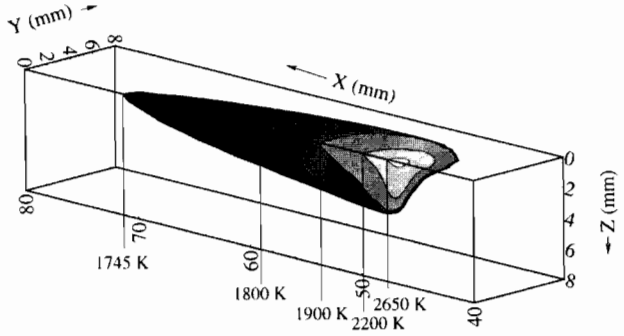

6 Calculated three-dimensional temperature distribution: welding velocity = 12·7 mm s^{-1}

Thermal conductivity of copper, J m^{-1} s^{-1} K^{-1}	334
Density of copper, kg m^{-3}	8920
Specific heat of copper, J kg^{-1} K^{-1}	418
Temperature coefficient of surface tension, N m^{-1} K^{-1}	$-0{\cdot}43 \times 10^{-3}$
Coefficient of thermal expansion	1×10^{-5}

Temperature values at the two faces are shown for purposes of clarity. In the solid region, the equation of conservation of energy was solved for both the steel specimen and the outer copper block. A thin air layer (6 μm) was also assumed to lie between the steel and the copper block.

The temperature field shows a typical elongated weld pool. The general features of the temperature field are consistent with the results reported in the literature. In front of the heat source, the temperature gradient is greater than that behind the heat source and the higher temperature gradient results in slightly greater velocities in front of the heat source than behind the heat source. This can be observed from the velocity fields on the weld pool surface and along the plane of symmetry ($y = 0$), plotted in Fig. 7. The weld pool surface flow shows that the liquid metal moves from the centre (point of maximum temperature) to the periphery of the weld pool. This is expected for a metal with a very low concentration of surface active elements, which results in a negative value for $d\gamma/dT$ over much of the weld pool surface. In the calculation, a constant, negative $d\gamma/dT$ value was assumed.

The effect of convection on heat transfer, for the welding conditions investigated, can be examined from the calculation of Pe_h, a measure of the relative magnitudes of convective and conductive heat transfer, given by

$$Pe_h = V_{max} L/\kappa \quad \ldots\ldots\ldots\ldots\ldots\ldots (14)$$

where V_{max} is the maximum velocity, L is the characteristic length that can be taken as the depth of the weld pool, and κ is the thermal diffusivity of the liquid metal given by

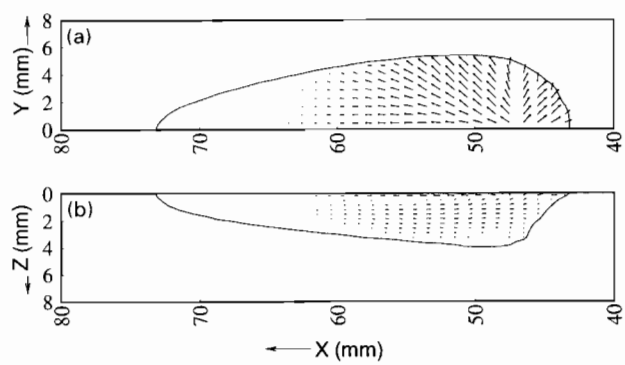

a on weld pool surface; *b* along plane of symmetry

7 Velocity fields: welding velocity = 12·7 mm s^{-1}

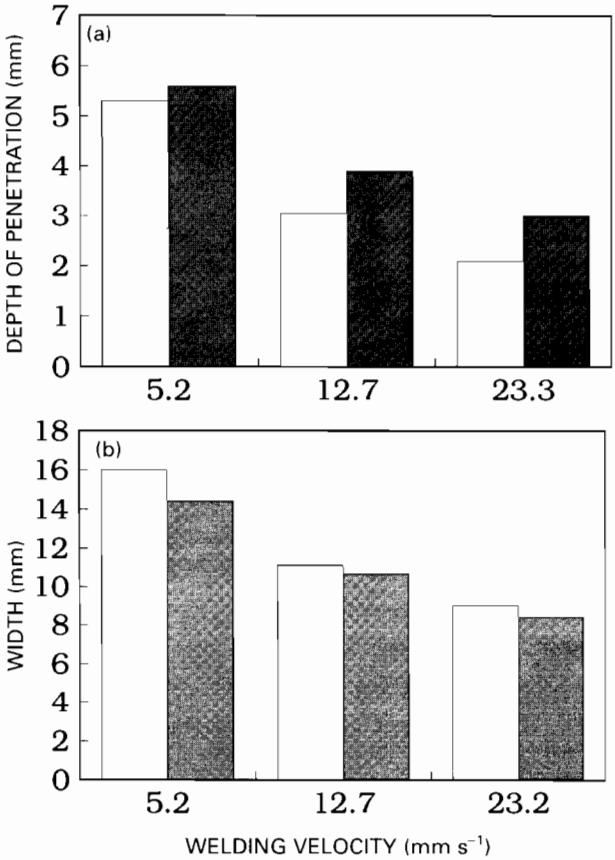

□ experimental; ■ calculated
a depth; *b* width

8 Comparison of weld pool size in given direction with experimental data for three welding speeds

$k/\rho c_p$, where k is the thermal conductivity of liquid and c_p is the specific heat. Using the values for parameters listed above, the weld geometry, and the maximum velocity in Fig. 7, Pe_h is found to be ~40. This high value ($\gg 1$) indicates that convection is the dominant mechanism for heat transfer under the conditions investigated for the GMAW of low alloy steels.

Weld pool geometry and thermal cycles

The computed weld pool depth and width are compared with the experimental results in Fig. 8. This comparison shows that the model predictions are in fair agreement with the experimental observations. The discrepancy between the experimental and the calculated depths can be attributed, at least in part, to the various assumptions involved in defining the heat source cavity that take into account the heat transfer to the weld pool from the metal droplets.

From the computed steady state temperature field, obtained by the solution of transformed momentum and enthalpy equations, temperature as a function of time at different locations can be calculated by making use of the equation[22]

$$T(x, y, z, t_2) = \frac{T(\xi_2, y, z) - T(\xi_1, y, z)}{\xi_2 - \xi_1} U_s(t_2 - t_1) + T(x, y, z, t_1) \quad \ldots\ldots\ldots (15)$$

where $T(\xi_2, y, z)$ and $T(\xi_1, y, z)$ are the steady state temperatures at coordinates (ξ_2, y, z) and (ξ_1, y, z) respectively, $\xi_2 - \xi_1$ is the distance travelled by the beam in the time $t_2 - t_1$, U_s is the welding velocity, and $T(x, y, z, t_1)$ and $T(x, y, z, t_2)$ are the temperatures at location (x, y, z) at times t_1 and t_2 respectively.

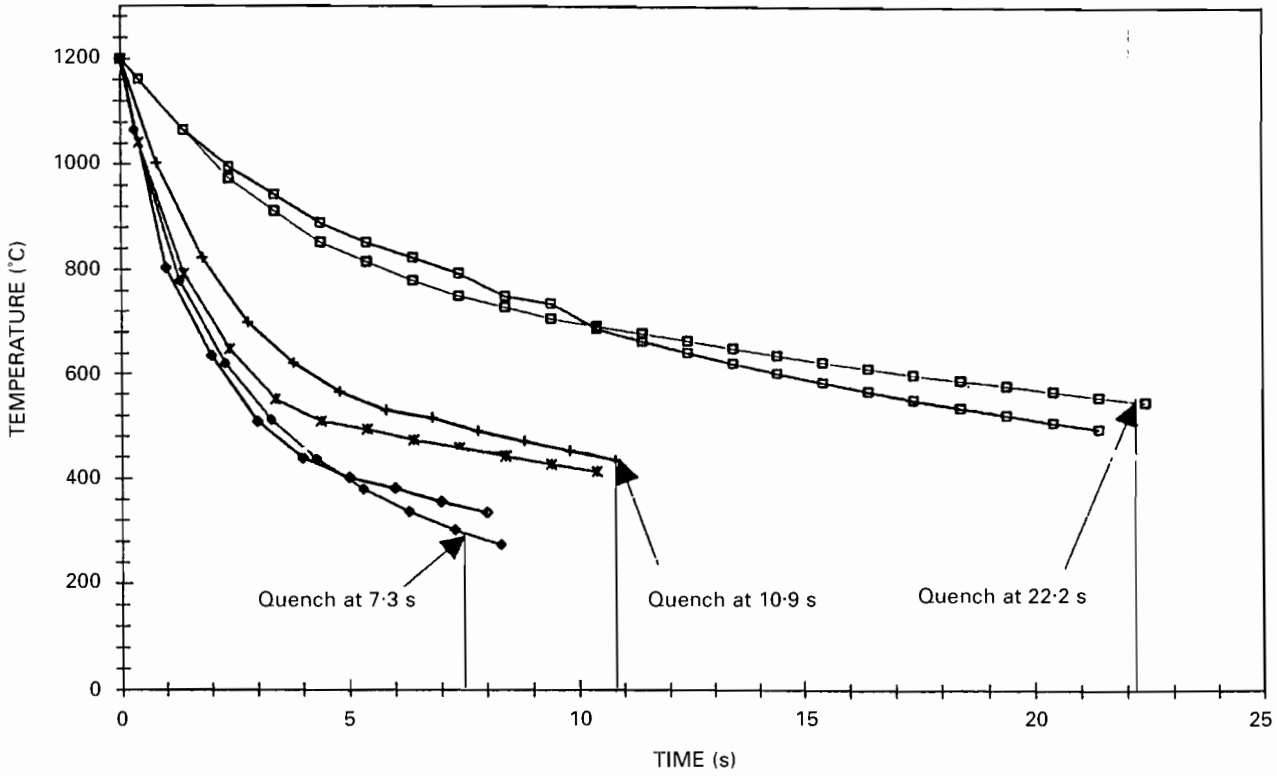

□ 5·2 mm s^{-1}; + 12·7 mm s^{-1}; ✳ 12·7 mm s^{-1}; ◆ 25·2 mm s^{-1}

9 Time–temperature data measured by thermocouple at weld centreline for given welding speed

The time–temperature data were measured experimentally by plunging a chromel–alumel thermocouple into the molten pool at the weld centreline at the end of the first test specimen when the arc was approximately half way through the second test specimen. This thermocouple was attached to a PC for data collection, which started when the temperature at the location where it was plunged reached just below 1200°C. The temperature–time data for the three welding conditions are shown in Fig. 9. From the experimental data, the time taken for the specimen to cool from 1200 to 500°C $t_{12/5}$ can be easily calculated. Experimental results and model predictions are compared in Fig. 10. The average of the two values for each welding velocity was taken as the experimental $t_{12/5}$. These results show that there is good agreement between the experimental observations and the model predictions and also show that $t_{12/5}$ decreases with an increase in the welding speed. This is expected because the heat source moves away faster from the heated region at higher welding speeds. Figure 11 shows the calculated peak temperatures as a function of welding speed. The results show that the peak temperature also decreases with an increase in the welding speed. Again, this is expected because at high speeds there is less time for interaction between the heat source and the material and, therefore, the temperature does not rise as much as for low speeds.

Hydrogen distribution in weldment

The role of convection in the distribution of hydrogen in the weldment can be measured from Pe_m, which is calculated using

$$Pe_m = V_{max} L/d \quad . \quad . \quad . \quad . \quad . \quad . \quad . \quad . \quad . \quad . \quad . \quad . \quad . \quad . \quad (16)$$

where d is the diffusivity of hydrogen. The value of Pe_m gives the relative measure of the convective and diffusive mass transfer. From Fig. 5, the diffusivity value in the

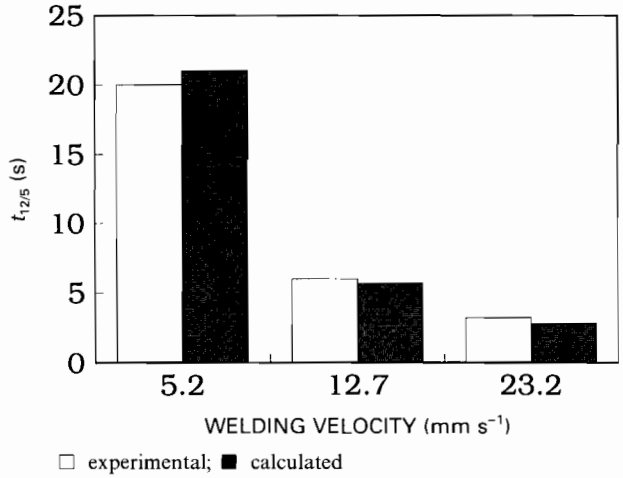

□ experimental; ■ calculated

10 Comparison of calculated and experimental $t_{12/5}$ values for three welding speeds

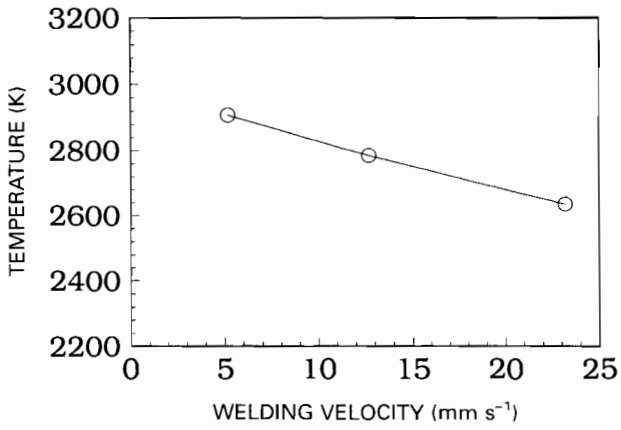

11 Calculated peak temperatures as function of welding speed

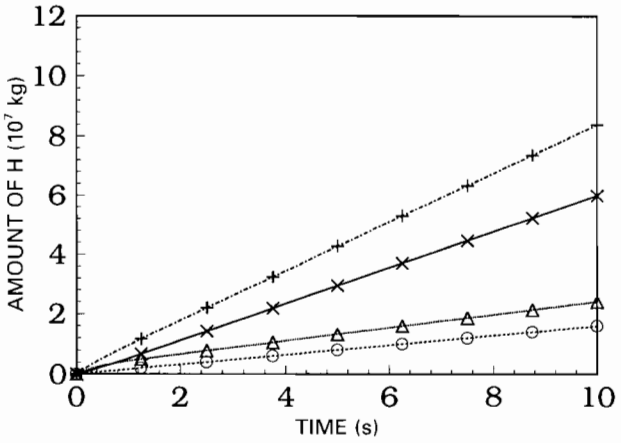

+ total transported into specimen; × total transported out of specimen; △ amount retained; ○ amount transported by droplets

12 Mass balance for H: welding velocity = 12·7 mm s^{-1}

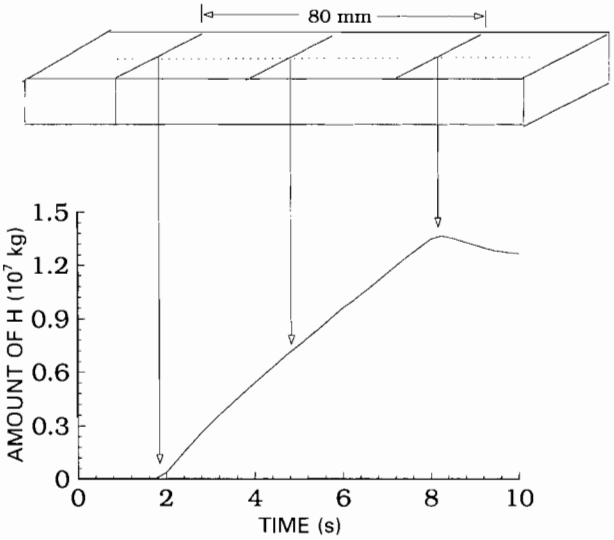

14 Amount of H in 80 mm test specimen as function of time: welding velocity = 12·7 mm s^{-1}

liquid phase is $\sim 1 \times 10^{-7}$ m^2 s^{-1}. From Fig. 7 the depth is calculated as 3·9 mm and the maximum velocity is 0·58 m s^{-1}. Substituting these values into equation (16), Pe_m has a value of 22 620 ($\gg 1$), which shows that convection is the dominant mechanism for the transport of hydrogen in the weld pool. Furthermore, an order of magnitude calculation of 'diffusion distance' for hydrogen transport can also be carried out using equation (13). The time that the pool remains molten at a welding velocity of 12·7 mm s^{-1} is $\sim$2·3 s (with a welding pool length of 29 mm) and welding velocity (of 12·7 mm s^{-1}). Taking the liquid phase diffusivity to be $1{\cdot}0 \times 10^{-7}$ m^2 s^{-1}, the computed diffusion distance, 0·9 mm, is small, showing that convection plays an important role in the transport of hydrogen in the weld pool.

The steady state velocity in the weld pool and the temperature distribution near the weld pool were both assumed to be valid for the entire duration of welding. Therefore, the hydrogen concentration calculations were performed using these velocity and temperature fields. The concentration calculations commenced in the start weld tab at a distance of 25 mm from the edge of the test specimen, where the arc was initiated, and finished in the end weld tab at a distance of 25 mm from the end of the second weld test specimen, where the arc was switched off.

The computed hydrogen balance for the entire specimen is shown in Fig. 12, which shows the total hydrogen transported into the specimen, the amount transported from the drops, the amount transported out of the specimen, and the amount retained in the specimen. Figure 12 shows that, in GMAW, a significant amount of hydrogen can be transported into the weld pool by the metal drops in addition to the amount absorbed at the weld pool surface. Both hydrogen desorption from the pool surface and its diffusion into the surroundings contribute to the hydrogen loss. A significant amount of hydrogen absorbed in the plasma region can be lost from the specimen surface in the region where the plasma is not present.

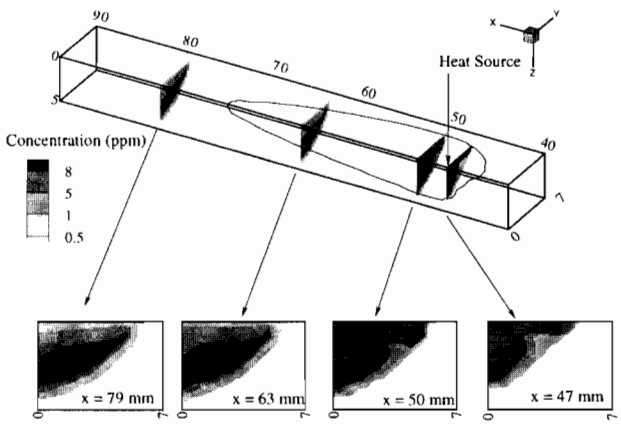

13 Calculated concentration of H at different planes in ξ direction: welding velocity = 12·7 mm s^{-1}

Concentrations of hydrogen at different planes in the ξ directions taken at the end of welding for the welding velocity of 12·7 mm s^{-1} are shown in Fig. 13; the molten pool geometry is also marked. The planes at $\xi = 47$, 50, and 63 mm are contained in the molten pool and Fig. 13 shows that the planes at $\xi = 47$ and 50 mm contain high concentrations of hydrogen throughout the entire section. This is because these planes contain the region where hydrogen transfer by droplets takes place and the surface is also exposed to monatomic hydrogen. In addition, transport of hydrogen by convection helps in the distribution of hydrogen. The planes at 63 and 79 mm have lower hydrogen concentration at the surface than the planes under the heat source. This is because these locations are away from the plasma and the volumetric hydrogen source in the pool. Here, the surface will tend to reach equilibrium with the diatomic hydrogen and a significant amount of hydrogen will desorb from the surface.

The variation in the amount of hydrogen in the two 40 mm test specimens (80 mm in total), as a function of time for the medium welding velocity case, is shown in Fig. 14. The results show that the hydrogen concentration starts increasing in the test specimens about 2 s after the start of welding. This is the time required for the heat source to traverse the starting tab (a distance of 25 mm at 12·7 mm s^{-1}). At the end of this period, the test specimen starts to melt and hydrogen transport from the metal drops and surface absorption takes place in the test specimen. After 8 s, the hydrogen concentration again begins to decrease in the test specimen. At this time the arc has passed the test specimen and is traversing the end tab. As a consequence, solidification of the test specimen begins and the surface absorption decreases considerably because of the absence of plasma. Furthermore, the hydrogen transfer from the droplet now occurs in the end weld tab.

The hydrogen concentration in the two 40 mm test specimens for the three welding velocity cases are compared

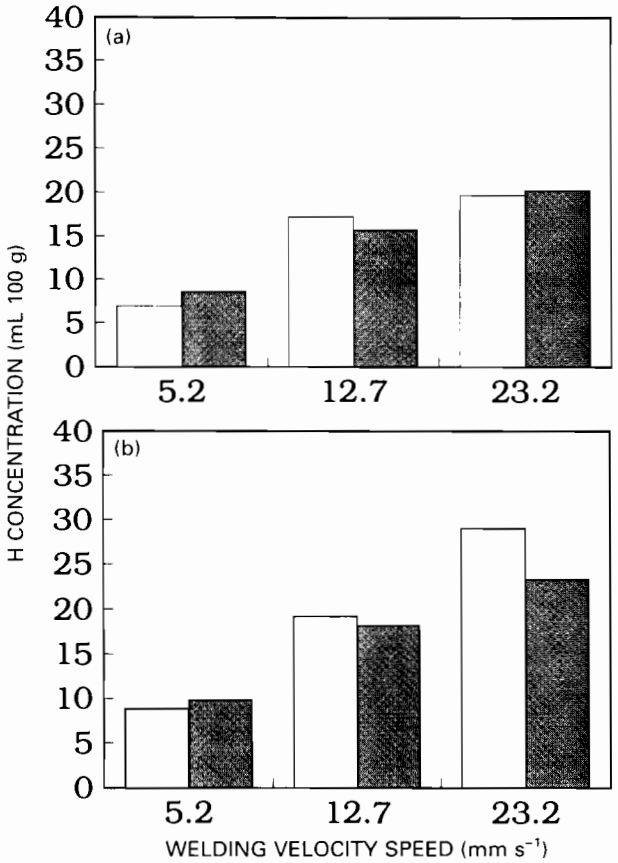

□ experimental; ■ calculated
a for first 40 mm specimen; *b* for second 40 mm specimen

15 Comparison of H content of test specimen with experimental results for three welding conditions

with the experimentally observed data in Fig. 15. To convert the amount of hydrogen in grams to mL/100 g of the deposited metal, it was necessary to use the relationship

$$C = 10^6(m_H/w)/0{\cdot}89 \quad \ldots\ldots\ldots\ldots \quad (17)$$

where m_H is the amount of hydrogen in the test specimen in grams, w is the deposited weight in grams, and 0·89 is the factor for the conversion of parts per million to millilitres/100 g of deposited metal.[1]

This comparison shows that the calculated results predict the trends fairly well, i.e. the hydrogen concentration expressed in millilitres/100 g of the deposited metal increases with increasing travel speed for both the test specimens. Furthermore, the lower concentration of hydrogen in the first test specimen (closer to the start weld tab) compared with that in the second test specimen (closer to the end weld tab) is consistent with the experimental observations.

CONCLUSIONS

A model to calculate heat transfer, fluid flow, and hydrogen concentration in the weldment in three dimensions has been applied to predict hydrogen concentration in the weldment for GMAW of steels. Heat and mass transfer from the metal droplets is taken into account by incorporating appropriate heat and mass sources in the weld pool. Numerical calculations show that convective heat transfer is important for determining the weld pool geometry. Geometry of the weld pool and cooling rates were found to be in good agreement with the experimental observations. The results show that convective mass transfer is important in determining the hydrogen distribution in the weld pool and the final hydrogen content in the weldment.

The predicted trend of the hydrogen content in the weldment, for the conditions investigated, is consistent with experimental observations. The results show that hydrogen content in millilitres/100 g of deposited metal increases with increasing welding velocity. Furthermore, the hydrogen concentration in the region which is welded first has a lower hydrogen content compared with the part that is welded last. The agreement between calculation and experiment shows that hydrogen absorption, desorption, and transport via the metal drops should all be considered when determining the residual hydrogen content and its distribution in the weldment. The calculations indicate significant promise for predicting weldment hydrogen content from the fundamental principles of transport phenomena for low alloy steels. Work is under way to apply the model for prediction of solubility of gases in the weld metal under various welding conditions.

APPENDIX 1

Momentum equation in moving coordinate system

The transient momentum equation in the ξ, y, z coordinate system is given by

$$(\partial/\partial t)\rho \boldsymbol{V} + \nabla\cdot\rho\boldsymbol{V}\boldsymbol{V} = -\nabla P + \mu\nabla\cdot\nabla\boldsymbol{V} + S + S_{e-p} - \nabla\cdot\rho\boldsymbol{U}\boldsymbol{V} \quad \ldots \quad (18)$$

where $\boldsymbol{V}$ is the convective component of the velocity, P is the effective pressure, μ is the viscosity, and $\boldsymbol{U}$ is the welding velocity. The source term S takes into account the buoyancy and electromagnetic forces and S_{e-p} is the source term that modifies the momentum equation in the mushy zone. For steady state, the first term in the equation is zero.

Energy equation

The energy equation is given by

$$(\partial/\partial t)\rho h + \nabla\cdot\rho\boldsymbol{V}h = \nabla\cdot(k/c_p)\nabla h - \nabla\cdot\rho\boldsymbol{V}\Delta H - \nabla\cdot\rho\boldsymbol{U}\Delta H - \nabla\cdot\rho\boldsymbol{U}h - (\partial/\partial t)\rho\Delta H + S \quad \ldots \quad (19)$$

where h is the sensible heat ($=\int c_p\,dT$), ΔH is the latent heat content, and S is the source term that takes into account the heat transfer from the metal drops. Again, for the steady state, the first and the last terms will be zero.

Conservation of hydrogen equation

The equation for conservation of hydrogen is

$$(\partial/\partial t)\rho C + \nabla\cdot\rho\boldsymbol{V}C = \nabla\cdot\rho D\nabla C - \nabla\cdot\rho\boldsymbol{U}C \quad \ldots \quad (20)$$

APPENDIX 2

Boundary condition for hydrogen concentration at weldment surface

The determination of surface concentration is illustrated with an example. Figure 16*a* shows the variation of the arc and weld temperatures at the top surface on the plane of symmetry for the welding velocity of 12·7 mm s^{-1}. For clarity, only the region near the weld pool is shown. From the arc temperature and the composition of the shielding gas, the partial pressure of the diatomic and the monatomic hydrogen can easily be calculated. The details of the methodology are given in a previous study by the present authors.[26] It can be seen from Fig. 16*b* that when the arc temperature is above 4000 K, almost complete dissociation of diatomic hydrogen takes place. The pressure of monatomic hydrogen reaches $1{\cdot}9 \times 10^3$ Pa for a feed gas containing 1% hydrogen. From the calculated partial pressures, equilibrium concentrations of hydrogen on the surface of the weld pool from the diatomic and monatomic hydrogen can be calculated from equations (6) and (8) respectively. These concentrations are shown in Fig. 16*c*. The predicted trend of concentration from monatomic

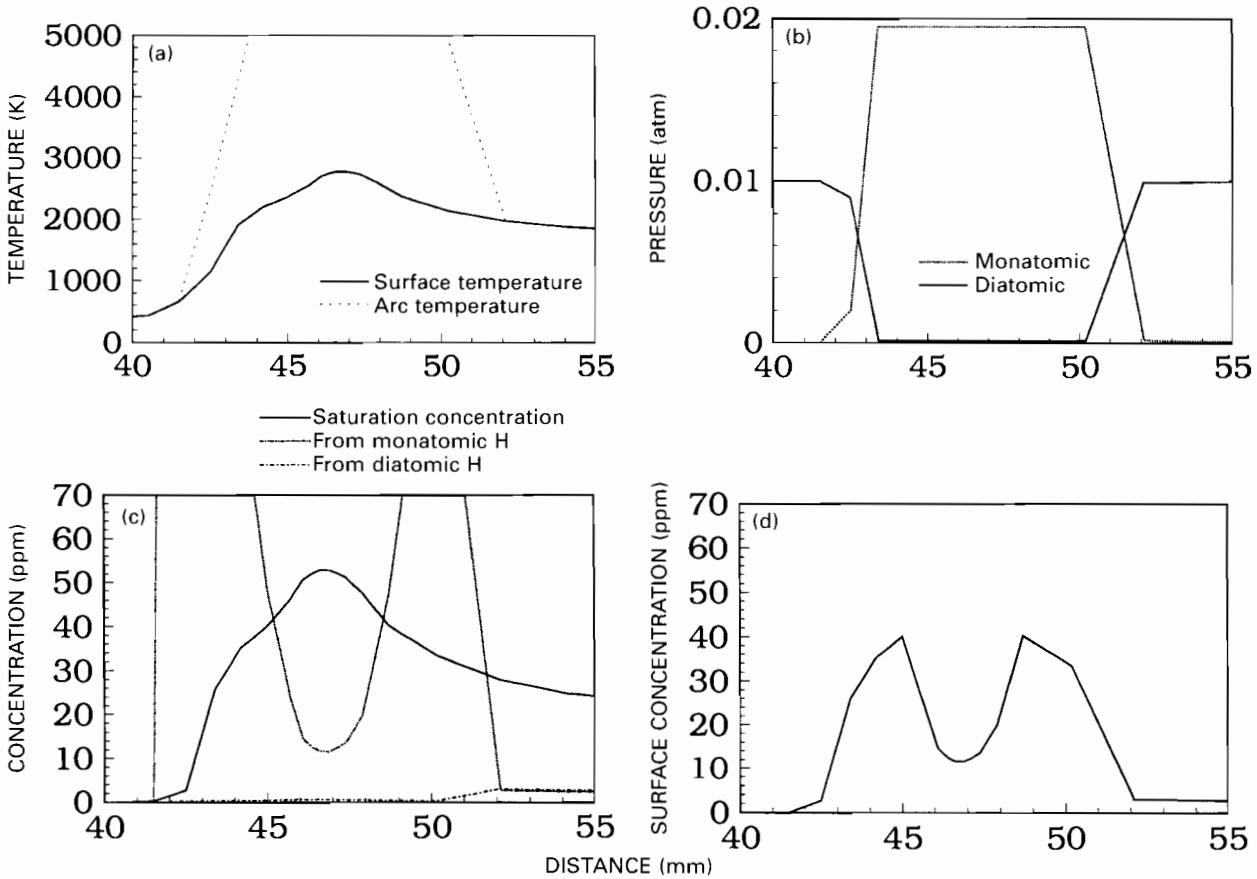

1 atm = $1{\cdot}013 \times 10^5$ Pa

a surface and arc temperatures; *b* partial pressures of monatomic and diatomic H; *c* concentration owing to monatomic and diatomic H and saturation concentration; *d* surface concentration at top surface on plane of symmetry

16 Variation of given parameters with welding distance: welding velocity = 12·7 mm s^{-1}

hydrogen is consistent with the results of Gedeon and Eagar,[1] which also showed that the surface concentration obtained from monatomic hydrogen is lower at higher surface temperature. When arc temperatures are low, there is an insignificant amount of dissociation of diatomic hydrogen. Under such conditions, the surface concentration is determined from the diatomic hydrogen. It is observed that the concentrations obtained from diatomic hydrogen are significantly lower than those obtained from monatomic hydrogen in the region where the dissociation of diatomic hydrogen takes place. Indeed, the surface concentration tends to be greater than the saturation concentration obtained from equation (12). At such a high concentration, nucleation of hydrogen bubbles will take place. Therefore, the surface concentration was limited to the saturation concentration. The resulting concentration of hydrogen at the surface of the weldment is shown in Fig. 16*d*.

ACKNOWLEDGEMENTS

The present work was supported by the US Department of Energy, Office of Basic Energy Sciences, Division of Materials Science under grant no. DE–FG02–84ER45158. Experimental work at the Naval Surface Warfare Center, Carderock Division was performed under the grant no. N61533–K–0060. The authors would like to thank T. A. Palmer for his comments on the manuscript.

REFERENCES

1. S. A. GEDEON and T. W. EAGAR: *Weld. J. Res. Suppl.*, 1990, **69**, (7), 264s.
2. M. UDA and S. OHNO: *Trans. Natl Res. Inst. Met. (Jpn)*, 1973, **15**, 20.
3. G. den OUDEN and O. GRIEBLING: in 'Recent trends in welding science and technology', (ed. S. A. David and J. M. Vitek), 431; 1990, Materials Park, OH, ASM International.
4. A. BANERJEE, T. DEBROY, C. ONNEBY, and M. SMALL: in 'International trends in welding science and technology', (ed. S. A. David and J. M. Vitek), 39; 1993, Materials Park, OH, ASM International.
5. T. TERASAKI, T. AKIYAMA, S. HAMASHIMA, and K. KISHIKAWA: *Trans. Jpn Weld. Soc.*, April 1986, 93.
6. I. G. DICKEHUT and J. RUGE: *Weld. Cast.*, 1988, **6**, 39.
7. T. BOELLINGHAUS, H. HOFFMEISTER, and A. DANGELEIT, *Weld. World*, 1995, **35**, (2), 83.
8. T. BOELLINGHAUS, H. HOFMEISTER, and C. SCHUBERT: Proc 4th Int. Conf. on Trends in Welding Research, Gatlinburg, TN, USA, June 1995, ASM International, 25.
9. W. PITSCHENEDER, T. DEBROY, K. MUNDRA, and R. EBNER: *Weld. J. Res. Suppl.*, 1996, **75**, (4), 71s.
10. W. PITSCHENEDER, M. GRUBÖCK, K. MUNDRA, T. DEBROY, and R. EBNER: Proc. 3rd Int. Seminar on Numerical Analysis of Weldability, Graz-Seggau, Austria, September 1995; in 'Mathematical modelling of weld phenomena 3', (ed. H. Cerjak), 41–63; 1997, London, The Institute of Materials.
11. K. C. MILLS and B. J. KEENE: *Int. Mater. Rev.*, 1990, **35**, (4), 185.
12. C. R. HEIPLE and J. R. ROPER: *Weld. J. Res. Suppl.*, 1982, **61**, 97s.
13. C. R. HEIPLE, J. R. ROPER, R. T. STAGNER, and J. J. ALDEN: *Weld. J. Res. Suppl.*, 1982, **61**, 72s.
14. A. PAUL and T. DEBROY: *Metall. Trans. B*, 1988, **19B**, 851.
15. 'Standard method for determination of the diffusible hydrogen content of martensitic, bainitic, and ferritic steel weld metal produced by arc welding', ANSI/AWS Standard A4.3–93, American Welding Society, Miami, FL, 1993.
16. S. V. PATANKAR: 'Numerical heat transfer and fluid flow'; 1980, New York, NY, Hemisphere.

17. Documentation for COMPACT-3D software, Version 3.1, Innovative Research Inc., Minneapolis, MN, 1194.
18. T. DEBROY and S. A. DAVID: *Rev. Mod. Phys.*, 1995, **67**, (1), 85.
19. S. KOU and Y. H. YANG: *Metall. Trans. A*, 1986, **17A**, 2265.
20. A. D. BRENT, V. R. VOLLER, and K. J. REID: *Numer. Heat Transfer*, 1988, **13**, 297.
21. V. R. VOLLER and C. PRAKASH: *Int. J. Heat Mass Transfer*, 1987, **30**, (8), 1709.
22. K. MUNDRA, T. DEBROY, and K. M. KELKAR: *Numer. Heat Transfer A*, 1996, **29**, 115.
23. Y. S. KIM and T. W. EAGAR: *Weld. J. Res. Suppl.*, 1993, **72**, (6), 269s.
24. S. KUMAR and S. C. BHADURI: *Metall. Mater. Trans.*, 1994, **25B**, 435.
25. J. N. DuPONT and A. R. MARDER: *Weld. J. Res. Suppl.*, 1995, **74**, 406s.
26. K. MUNDRA and T. DEBROY: *Metall. Mater. Trans.*, 1995, **26B**, 149.
27. A. BANDOPADHYAY, A. BANERJEE, and T. DEBROY: *Metall. Trans. B*, 1992, **23B**, 207.
28. J. F. KEY, J. W. CHAN, and M. E. McILWAIN: *Weld. J. Res. Suppl.*, 1983, **62**, 180s.